Effect of seawater on solidification/stabilization treatment of marine soft soil slurry by lime-activated ISSA and GGBS

Zhao SUN[1, 2], Wen-Bo CHEN[1, 3], Run-Dong ZHAO[1], Peiliang SHEN[1], Jian-Hua YIN[1], Yong-gui CHEN[2]

[1]*Department of civil and environmental engineering, The Hong Kong Polytechnic University, Hung Hom, Kowloon, Hong Kong, China.*

[2] *Department of Geotechnical Engineering, School of Civil Engineering, Tongji University, Shanghai, China.*

[3] *College of Civil and Transportation Engineering, Shenzhen University, Shenzhen, Guangdong, China.*

Corresponding author: Wenbo CHEN

Email : wenbochen@polyu.edu.hk; geocwb@gmail.com

Phone : 852-3400 8075

Abstract

It is proposed to use dredged marine sediments as fill material in marine reclamation engineering by stabilisation/solidification (S/S) technology with sustainable binding material, which can help the soft soil gain strength to solve the engineering geological problem of its insufficient bearing capacity. In this work, lime and two types of industrial wastes, i.e., incinerated sewage sludge ash (ISSA) and ground granulated blast-furnace slag (GGBS), were selected as the binding materials. Hong Kong marine deposits (HKMD) slurry with a high initial water content of 110% was mixed with 30% binders (30% lime and 70% (ISSA+GGBS) with ISSA: GGBS=3). The seawater (SW) with salinity of 3.6% was employed as mixing solution in S/S treatment of HKMD. To detect the effect of each main composition in SW on the performance of S/S HKMD, the pure solutions of NaCl, $MgCl_2$ and Na_2SO_4 were adopted in this study. The results show that the use of SW in the lime-activated ISSA and GGBS treated dredged HKMD slurry is effective in improving its strength. The X-ray diffraction, thermo-gravimetric analysis and scanning electron microscopy observations present the formation of calcium/magnesium silicate hydrate (C/M-S-H), Friedel's salt, and ettringite, which are mainly responsible for the strength increase of the treated HKMD because of these phases filling into the pores and interlocking the particles in the mixture. The chemical compositions in the mixing solutions have significant and different impacts on the performance of treated HKMD samples. Na^+ can help the samples gain higher strength and result in the crack increasing in the S/S samples. Mg^{2+} in the mixture will lead to the formation of M-S-H, which reduces the porosity of treated HKMD samples. However, the contribution of M-S-H to the strength of treated HKMD is less than that of C-S-H. Cl^- in the mixture would slow down the reaction speed in the system and show slight impacts on the modulus. Sulfate ion accelerates the reactions in the treated samples and has a more significant effect on nano-size porosity of bulk sample. Consequently, the seawater has positive effect on the S/S performance of HKMD slurry, suggesting potential application in the practical projects.

Keywords: Reclamation engineering, soft soil, stabilisation/solidification, incinerated sewage sludge ash, ground granulated blast-furnace slag, seawater

1 Introduction

As a typical geological stratum in Hong Kong waters, the granite bedrock is decomposed to depths approximately 70 m beneath the current seabed. The percolation of fresh water facilitates the decomposition of granite at rock joints. A layer of alluvium, ranging from 30 m to 60 m thick, is resulted from freshwater deposits of interbedded alluvial clay and sand formed on stream beds and flood plains. The uppermost layer is a 10 to 20 m thick marine sediments, which are essentially derived from the erosion of decomposed granite and rhyolite and transported by Pearl River. In order to maintain the marine ecological environment and offshore engineering construction, dredging is frequently carried out to remove part of the sediments. In Hong Kong, 29 Mm^3 dredged marine sediments are produced per year (Zhou et al., 2021a). Due to high water content and low permeability of the newly blow-filled soft soil, stabilisation/solidification (S/S) has become an important remediation technology to improve the strength of soft soil in order to achieve add-value recycling of the dredged marine sediments into competent construction materials, e.g., fill materials in marine reclamation. Incinerated sewage sludge ash (ISSA) as an industrial waste is coming from the incineration of dewatered sewage sludge. There is about 1200 tonnes of dewatered sewage sludge per day in Hong Kong, which raises an urgent issue of identifying suitable disposal sites for ISSA. In addition, the ground granulated blast-furnace slag (GGBS), another industrial waste, which is a by-product of iron manufacturing and could be used to improve the strength, workability and durability of S/S treated soft soil.

Nowadays because of the shortage of freshwater, there has been increasing concern about water use. According to World Meteorological Organization (Nishida et al., 2015), the drinking water is predicted not enough by the year 2025 for over 50% of the world's population. For saving freshwater, scholars have been exploring the possibility of using seawater (SW) in concrete (Dhondy et al., 2019). This study attempts to position the seawater as a potential alternative to freshwater for S/S treatment of HKMD. Especially for a project in marine environment, it will be more economical, environmentally-friendly and resource saving. This work tries to reveal the effect of seawater on lime-activated ISSA-GGBS binding HKMD slurry.

ISSA is a granulate waste with porous structure and large surface area (Pan et al., 2003). Zhou et al. (2020) investigated the application of ISSA as a stabilisation agent in S/S soft soil and found that the pozzolanic activity of ISSA is moderate. Jagaba et al. (2019) investigated that adding 7% ISSA can significantly improve the unconfined compressive strength (UCS) of clay soil with optimum water content of 16 %. A soft subgrade soil with optimum water content of 16.5-18 % increases its UCS with the increasing dosage of ISSA/hydrated lime ranging from 2% to 16%. It is pointed out that C-S-H hydrates make soil particles denser and crystallized ettringite phases were noticed (Lin et al., 2007). GGBS as another industrial waste, possessing a relatively low price of about 60-80% Portland cement price in China (Yi et al., 2015), which would produce less CO_2 emissions approximately of 0.07 tonne for 1 tonne of GGBS comparing to 0.95 tonne for Portland cement (Higgins, 2007). Celik and Nalbantoglu (2013) carried out tests on lime-GGBS stabilized sulfate bearing clays, and found that the treated soil with water content of 23-26 % gained significantly higher plasticity with the formation of needle-like ettringite minerals. Yi et al. (2015) compared lime–GGBS with Portland cement in soft clay stabilization with initial water content of 60%. It was found that the optimum UCS of hydrated lime–GGBS stabilized sample at 90-day was 1.7 times that of the Portland cement stabilized sample. The results also reveal that the main hydration products were C-S-H and alumino-ferritemonosulfate (AFm), which could reduce the porosity of treated clay. These formations improve the mechanical behaviour of dredged sediments (Zentar et al., 2012).

As to the influence on the performances of concrete when using seawater, a review study by Zhao et al. (2021) concluded that seawater can accelerate the strength gain of concrete at early ages. Some studies introduced metakaolin as pozzolanic materials in seawater concrete increasing the chloride resistance by the formation of Friedel's salts (Li et al., 2015; Shi et al., 2015). Zhou et al. (2021) studied the effect of seawater on the S/S treated sediments, and found that seawater can accelerate and promote the strength development of the lime-ISSA binder. The strength of the lime-ISSA paste mixed with seawater at 28-day was more than double that of mixed with freshwater.

As the main cation in seawater is Na^+ and Mg^{2+}, and its main ion is Cl^- and SO_4^{2-}, the effect of main chemical compositions such as NaCl, Na_2SO_4, $MgCl_2$ on concrete or other mixture is necessary to be investigated. The preferential reaction of sulfate ions with 3CaO Al_2O_3 produces ettringite, which would inhibit the formation of Friedel's salt (F's salt) (Dehwah et al., 2003). Moreover, it seems that ettringite display higher stability than F's salt (Xu et al., 2013). It was found that Cl had a detrimental impact on the strength of the cement-stabilized clay. Additionally, NaCl in the soil can react with the stabilizer forming F's salt, and thus increase the strength of stabilized soil significantly (Cheng et al., 2017). Gypsum and alumina-bearing phases can be used as stabilizer for some kinds of soil due to the formation of AFt in the stabilized soil, and further improve the strength (Wild et al., 1998). Brown and Badger (2000) found that in Na_2SO_4 solution, F's salt can convert to ettringite. During this conversion, it is expected that the chemically bound chloride can be released to free chlorides. In addition, the sulfate ions may compete with the chloride ions to adsorb on the C-S-H phase physically releasing physically bound chlorides (Xu et al., 2013). Yi et al., (2014) found that the MgO–GGBS stabilized clay was nearly inert to this sodium sulfate solution for the clay with initial water content of 80%.

Magnesium can react with silica from the cement leading to form the magnesium silicate hydrate (M-S-H) under saturated conditions of mixture (Jenni et al., 2014; Dauzeres et al., 2016). $MgCl_2$ can lower the pH of paste, and then hinder the C-S-H formation and facilitate the M-S-H formation (Kim et al., 2022). The $Mg(OH)_2$ precipitation will consume certain amount of $Ca(OH)_2$, which would decrease the alkalinity of the pore water, and thus reduce the stability of C-S-H. Besides, Mg^{2+} could also react with C-S-H directly forming M-S-H (Luo et al., 2019).

This work aims to study the effect of seawater on S/S performance of Hong Kong marine deposits (HKMD) slurry with a high initial water content of 110% treated by lime-activated ISSA and GGBS binder. Considering the practical application related to the rapid solidification of dredged soft soil, it is an effective and time-saving method to cure and stir the dredged soil with a high water content directly after dredging. In view of the variety of materials and chemical components in the mixed system, the reactions are very complex. This study attempts to reveal the effect of the components in seawater on

the S/S HKMD and its mechanisms. As the main cation in seawater is Na^+ and Mg^{2+}, and its main ion is Cl^- and SO_4^{2-}, the chemical agents including NaCl, $MgCl_2$ and Na_2SO_4 and seawater of 3.6% salinity were selected to prepare the solutions. UCS, X-ray diffraction (XRD), thermo-gravimetric (TG) analysis, scanning electron microscopy (SEM), mercury intrusion porosimetry (MIP) technique and nitrogen adsorption/desorption isotherms (NAI) tests were performed to analyse the treated samples for the macro-property, material characteristic, and microstructure through a combination of nano- micro- and macro- scale investigations. This research aims at new findings by multiscale investigations on hydration mechanisms of S/S treatment of soft soil slurry in marine geological engineering with particular emphasis on the effect of seawater.

2 Materials and Methodology

2.1 Hong Kong Marine Deposits and Binders

HKMD was collected from a dredging site located near Lamma Island, Hong Kong. The basic parameters of dredged HKMD were tested according to Geospec 3 shown in Table 1 (HK CEDD, 2017). The main compositions (mass fraction) of the raw HKMD include: quartz 55%, kaolinite 14.4%, muscovite 11%, halite 8.3%, albite 4%, phillipsite 3.7%, etc. The binders include lime (96.7% CaO), ISSA collected from a local sewage sludge incinerator, and GGBS from Wuhan Iron and Steel Plant. The ISSA and GGBS were oven-dried at 105 °C overnight in advance. The major oxide compositions of the binders were examined by X-ray fluorescence (XRF, Rigaku Supermini 200) listed in Table 2. A laser particle size analyser (Mastersizer 3000, Malvern, U.K.) was employed to determine the particle size distribution of HKMD, ISSA and GGBS with the results shown in Fig. 1, and SEM images of the three materials at a raw state are shown in Fig. 2.

Table 1. Basic properties of Hong Kong marine deposits (SSA: specific surface area).

G_s	Plastic limit (%)	Liquid limit (%)	PI	BET SSA (m^2/g)	pH
2.53	33	50	17	12.94	7.54

Table 2. Major chemical compositions of ISSA, GGBS and lime (wt. %).

	SiO_2	Al_2O_3	CaO	Fe_2O_3	MgO	K_2O	Na_2O	P_2O_5	SO_3	TiO_2
ISSA	22.3	12.0	10.3	17.6	3.94	1.95	12.8	10.0	6.90	0.641
GGBS	29.3	15.1	43.7	0.37	7.91	0.352	-	0.101	2.11	0.589
Lime	1.4	0.587	96.7	0.186	0.712	0.06	-	0.132	0.158	-

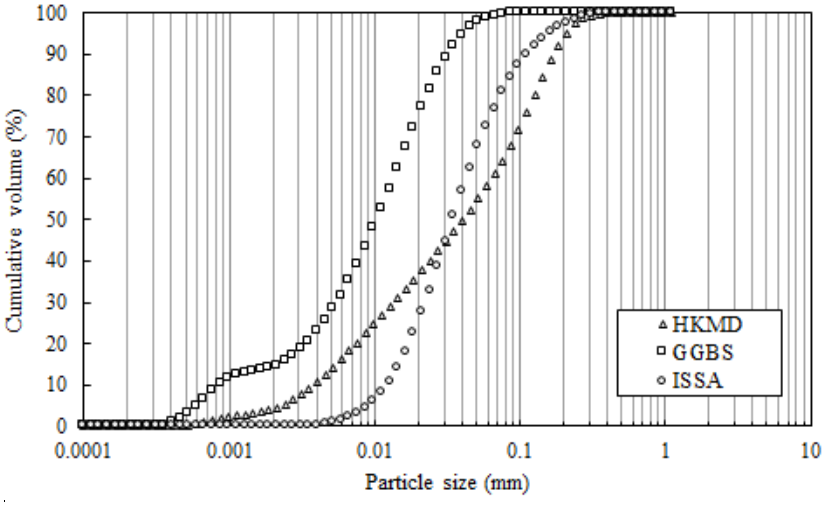

Fig. 1. Particle size distribution curves of the three materials.

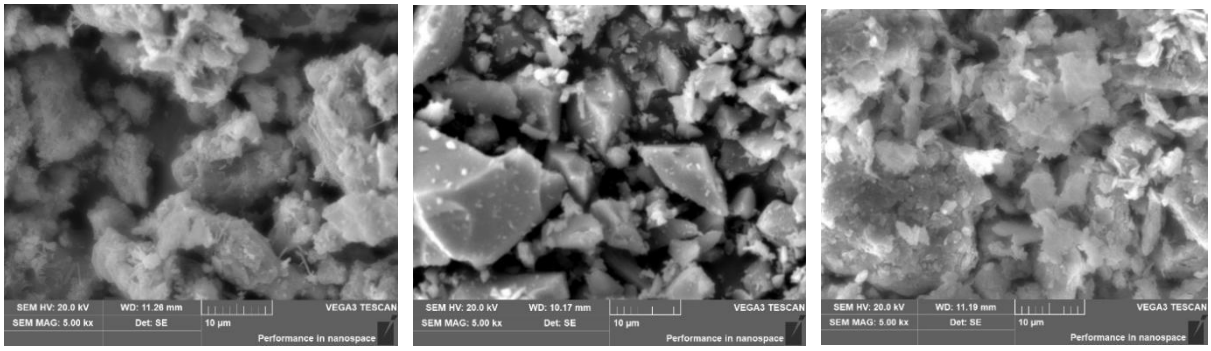

(a) (b) (c)

Fig. 2. SEM images of the three materials: (a) ISSA, (b) GGBS, and (c) HKMD (5 kx).

2.2 Mix design and sample preparation

The proportions of binders (lime, ISSA and GGBS) was selected as 30%, in which the ISSA and GGBS (ISSA to GGBS ratio 3:1) were mixed with lime powder in a mass ratio of 7:3. The initial water content of HKMD was adjusted to 110% by adding synthetic seawater with salinity of 3.6%. The compositions

of seawater employed in this work is listed in Table 3, in which the concentration of Cl^-, Na^+, Mg^{2+} and SO_4^{2-} is 0.529, 0.465, 0.055 and 0.028 mol/L, respectively. The chemical agents including NaCl, $MgCl_2$ and Na_2SO_4 of 3.6% salinity were also prepared for use, with the concentration of 0.615, 0.379 and 0.254 mol/L, respectively. Before being added into the HKMD slurry, the dry binders were firstly mixed thoroughly. Then, the mixture was stirred in a blender for 5 mins until reaching homogeneity. After that, the fresh mixture was put into cylindrical plastic moulds of 100 mm in height and 50 mm in diameter, which was shaken on a shaking table for about 2 min to remove air bubbles in the mixture. Finally, all the moulds with mixture wrapped in plastic films were kept in a chamber at 20 ± 2 °C and 97 % of humidity. The specimens would be demoulded after 7-day curing, and then sealed by plastic films curing in the environmental chamber for a predetermined period.

Table 3. Composition (in mg/L) of Red Sea salts prepared at 36 g/L

Compound	Cl	Na	Mg	S	Ca	K	C (inorg)	Br
Concentration (mg/L)	18,772	10,691	1320	890	480	390	45	15

2.3 Testing methods

2.3.1 Unconfined compressive strength

The unconfined compression tests were carried out on the cylindrical samples after 28-, 56- and 91-days curing using a triaxial compression machine (VJ-Tech Tri-Scan 50) with strain rate at 1 mm/min. A load cell fixed on the compression frame was employed to measure the axial loading. The global vertical strain was measured by a 50 mm linear variable differentiate transformer (LVDT) and the local vertical strain was measured by two 5 mm LVDTs. The specific setup is described in Ho et al. (2021). The water content of the treated samples was determined after being oven-dried at 105 °C for 24 h, and the average of triplicate data was used for analysis.

2.3.2 Mineralogy and Microstructure characteristics

After 28 and 56 days of curing, the parallel specimens were frozen-dried (-85 °C, 0.133 mbar) in a freeze-drier (Labconco Freezone 2.5 Plus) for 48 h. Then, the frozen samples were ground into fine powders for the XRD, TG, and NAI analysis. An X-ray diffractometer (Shimadzu XRD-6000, Japan) operating at 30 mA and 40 kV was used in the investigation of treated HKMD samples with CuKα radiation (λ = 0.154 056 nm). The 2θ range from 5 to 70 ° with a 0.02° step interval was selected during the tests. The identification of peaks was performed by the Jade software with the database ICDD PDF 2013. TG analysis (Netzsch STA 449F3) was conducted on the frozen-dried powder with the amount of around 10 mg. The testing temperature was ranging from 30 to 1000 °C with 10 °C/min heating rate and 50 mL/min flow rate of the nitrogen gas to prevent carbonation of samples.

Because of the multi-scale feature of pore sizes ranging from nano-meter to micro-meter in the treated HKMD, it is impossible to use a single technique to obtain a complete PSD. Thus, multiple techniques including MIP, NAI and SEM tests were carried out in this study to quantify the microstructure characteristics of the treated HKMD, which allows different scales of microstructure analyses conducted. The MIP (Micromeritics Autopore V 9600) method was used to measure the pore size distribution and porosity of the frozen S/S treated HKMD samples in the block state. A TriStar II 3020 surface area and porosity analyzer (Micromeritics Instruments Corporation) was employed to carry out the NAI tests for detecting the nano-structure of the treated HKMD powder, during which the relative pressures (p/p_o) range from 0.05 to 0.99 at the liquid nitrogen temperature of -196 °C. The morphologies and microstructure of the S/S HKMD samples were analysed by SEM in the secondary electron (SE) mode (TESCAN VEGA 3).

3 Results

3.1 Strength of S/S treated HKMD

The stress–strain curves of treated HKMD samples with four kinds of mixing solutions at different curing times are presented in Fig. 4. It can be observed that all the treated samples with four kinds of

mixing solutions have significantly gained unconfined compressive strength (UCS), which generally increases with curing time. It is also seen that the treated HKMD samples display obvious strain softening behaviour. It should be noted that the UCS of treated HKMD samples is not up to a high level, which is mainly due to the high initial water content, as it is a main factor influencing the strength of the treated HKMD. In addition, the treated samples exhibit a higher strength with increasing curing time. Considering the initial HKMD slurry with no strength before being treated, it indicates that the binders of lime-activated ISSA and GGBS are effective in improving strength of HKMD slurry and the Na_2SO_4 contributes most in the S/S process of treated HKMD. It is indicated that the 56- and 91-day curing samples with mixing solution of Na_2SO_4 or SW have a similar strength, respectively, which suggests much faster modification reactions such as pozzolanic reaction and hydration reaction occurred in these mixtures while comparing the SW mixed system with the distilled water mixed one (Zhou et al., 2022). The secant modulus degradation curve is shown in Fig. 5 with the data based on the global and local axial strains (Ho et al., 2021). The data with strain level from 0.01% to 1% are obtained from local LVDTs, which are believed more reliable in small strain determination. While for the strain larger than 1%, the results from global LVDTs were adopted. It is shown that the curves resulting from these two kinds of LVDT overlap at the strain level of around 1%, constituting a smooth curve, which indicates the reliability of the measurement from the two LVDTs. Additionally, the secant modulus for strain within 0.1% improves significantly while the curing time increasing from 28 to 91 days, except in the case of samples with hydration solution of NaCl. On the contrary, the difference in modulus diminishes gradually with the increasing strain level and finally converges to a similar value within the residual shearing stage. The specific data of the UCS of each sample hydrated by the different kinds of solution is shown in Fig. 6(a). It is obvious that the UCS of the samples is following the order of $MgCl_2$<SW<NaCl<Na_2SO_4, which means that the chemical compositions, like NaCl and Na_2SO_4, play a positive role on the strength improvement of the S/S treated HKMD slurry, while on the contrary, $MgCl_2$ plays a negative role in this aspect. According to Fig. 6(a), the samples with SW and Na_2SO_4 gain 98-100% strength at 56 curing days, which is in agreement with the result in Younis et al. (2018) that the strength of seawater-mixed concrete kept growing up to 56 days. While in the other two cases, the strength increases in the treated samples mixed by $MgCl_2$ and NaCl solutions continue to 91 days

and the strength at 56 days is about 83-85% of that at 91 days. It indicates that the reaction involved in chloride ions lasts longer than sulfate. It means that compared with chloride ion, sulfate ion accelerates the reactions in the treated samples relatively.

The modulus E_{50} is defined as the secant modulus at 50% of UCS, which is an important parameter in evaluating deformation behaviour of the treated soils. The E_{50} results of the S/S treated HKMD samples with four mixing solutions at different curing times are presented in Fig. 6(b). It is obvious that the modulus of the samples with $MgCl_2$ and NaCl almost keeps constant with the curing time increasing from 28 to 91 days, even the strength increases in the samples with $MgCl_2$ and NaCl with time (Fig. 6(a)). It can be deduced that Cl^- has little effect on the modulus of samples. On the contrary, the modulus of the samples with SW and Na_2SO_4 keeps increasing with time, which suggests that SO_4^{2-} has positive impact on improving the modulus of samples.

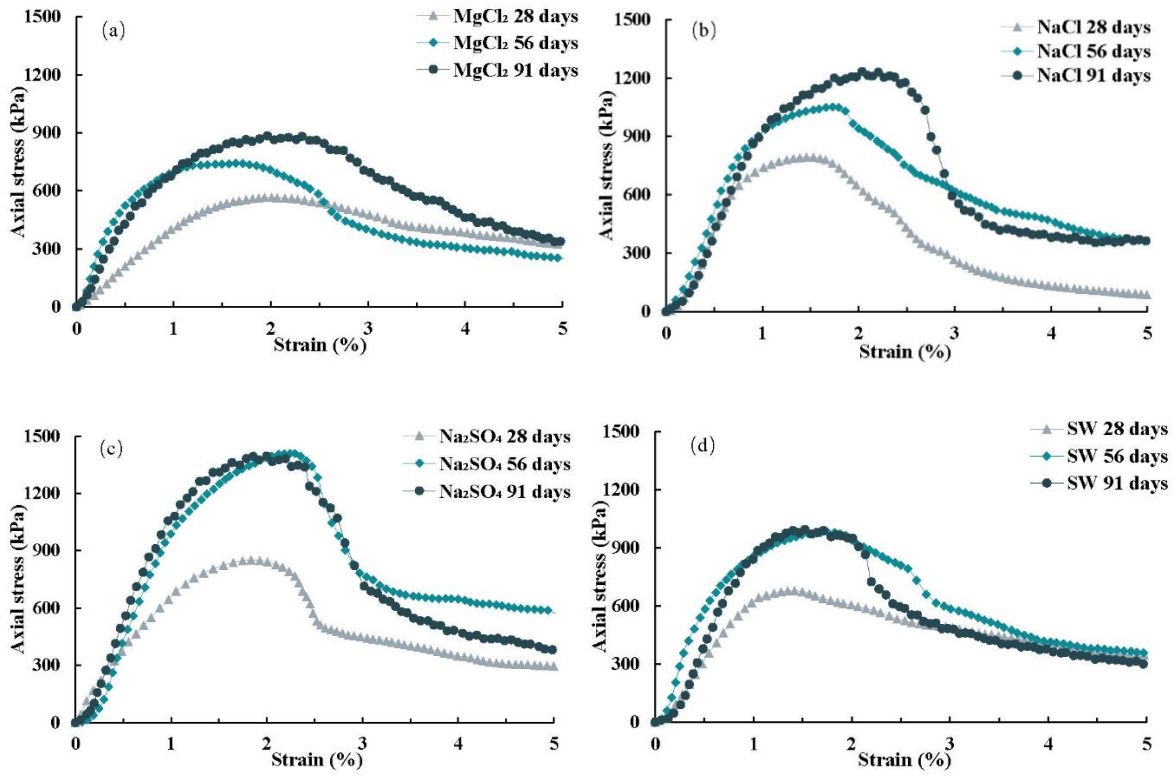

Fig. 4. Strain-stress curves of the treated samples.

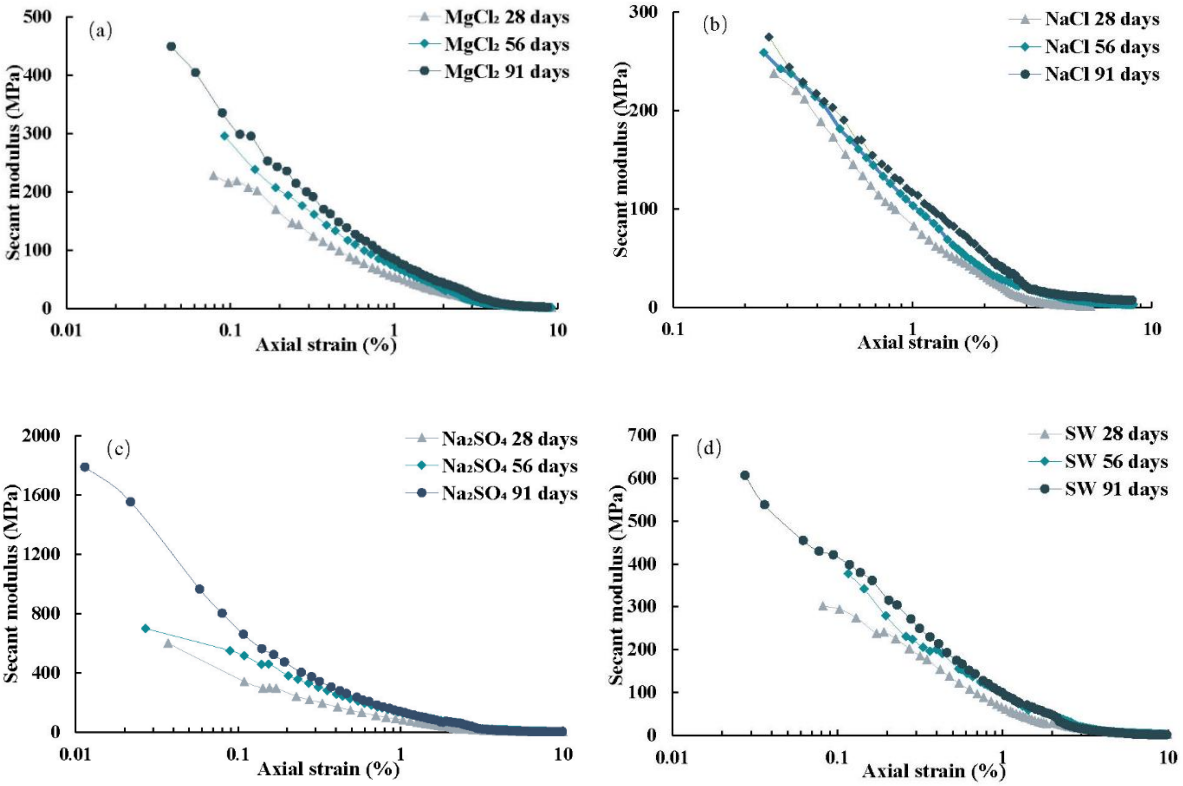

264

265

266 Fig. 5. Relationship between strain and modulus of treated samples.

267

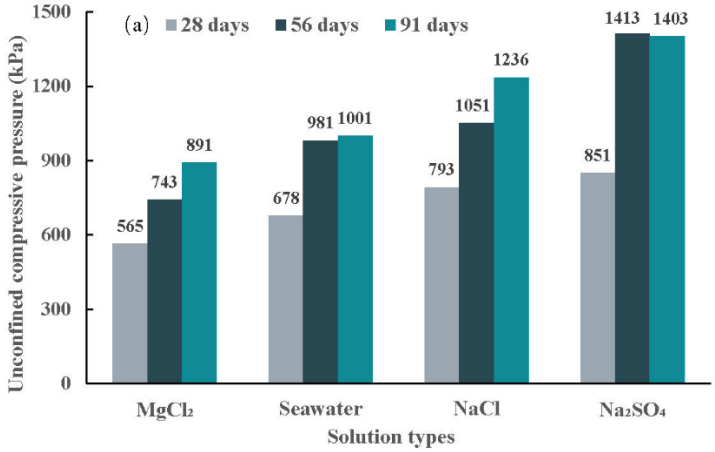

268

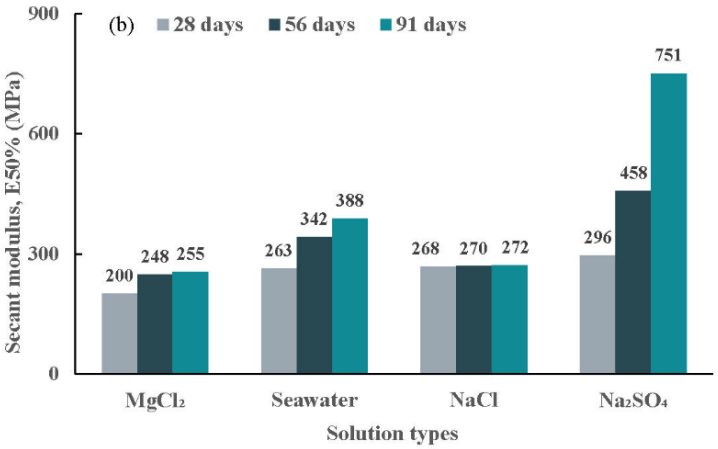

Fig. 6. The macro-property of treated samples under different solutions

3.2 XRD analysis

The XRD patterns of raw HKMD and lime-activated ISSA-GGBS modified HKMD samples mixed with 3.6% salinity $MgCl_2$, NaCl, Na_2SO_4 and SW solutions at 56 curing days are presented in Fig. 7. Besides the main compositions in HKMD, several representative hydration phases were depicted in the S/S treated HKMD samples, including calcium silicate hydrate (C-S-H) minerals, Friedel's salt (F's salt), and ettringite (AFt). The ettringite is recognized by its peak at 3.24 Å (2θ = 27.474°) in treated samples, which indicates that some of the ettringite is crystalline. F's salt is indicated by the peaks at 7.89 Å (2θ = 11.205°), 2.87 Å (31.137°), 2.52 Å (35.597°) and 1.979 Å (45.813°) in the S/S samples. It is found that the peaks of the halite (NaCl) in raw HKMD at 2θ of 31.68° (2.82 Å) and 45.42° (2 Å). The intensity of these peaks decreases or even disappears in the XRD patterns of the treated samples, which suggests that the halite dissolves under the high water content conditions in the curing process. This would provide chloride ions in the system favouring the formation of F's salt.

The formation of F's salt is probably following Equation (1) (Zhou et al., 2021a):

$$3Ca(OH)_2 + CaCl_2 + Al_2O_3 + 7H_2O \rightarrow 3CaO \cdot Al_2O_3 \cdot CaCl_2 \cdot 10H_2O \text{ (Friedel's salt)} \quad (1)$$

In addition, the formation of ettringite is mainly due to Equation (2) (Min et al., 2019):

$$6Ca(OH)_2 + 3(SO_4^{2-})\text{(dissolution of sulfate ions)} + Al_2O_3 + 29H_2O \rightarrow 3CaO \cdot Al_2O_3 \cdot 3CaSO_4 \cdot 32H_2O \text{ (ettringite)} + 6OH^- \quad (2)$$

In this work, the MgO in ISSA would react with water during the hydration process in the curing period releasing the Mg^{2+} and OH^-. It was reported that C-S-H and possibly M-S-H gels can be formed relating to the Ca^{2+}, Mg^{2+} and OH^- concentrations in the cement-based material and fly ash system (Wang et al., 2019). C-S-H is detected by peaks at 3.52 Å (25.279°), 2.81 Å (31.778°), 2.56 Å (35.018°), 2.21 Å (40.799°) and 1.63 Å (56.356°) in the S/S samples. Although the structure of M-S-H is unknown, it was reported that at lower Mg/Si ratio the M-S-H structure is related to a disordered talc ($3MgO{\cdot}4SiO_2{\cdot}H_2O$) (Lothenbach et al., 2015; Roosz et al., 2015), which demonstrates that the peak of talc can represent low crystalline M-S-H phases. The peak on the XRD patterns with an interlayer distance of 1.63 Å may be due to talc, which is overlapping with the peak of C-S-H indicating the possible coexistence of C-S-H and M-S-H.

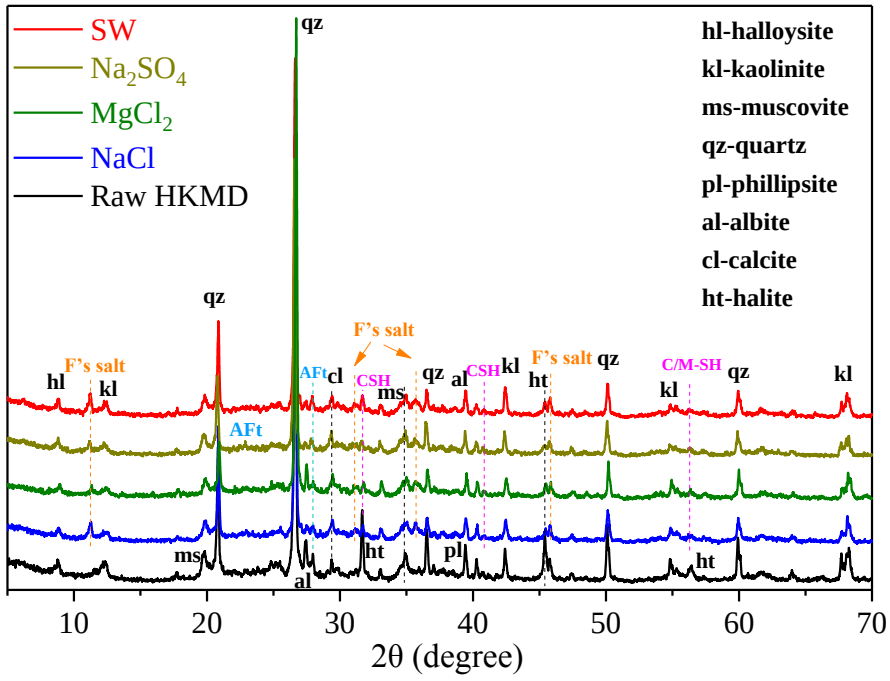

Fig. 7. XRD spectra of samples before and after 56 days of S/S treatment (F's salt: Friedel's salt, AFt: ettringite).

3.3 TG analysis

The TG and DTG results of S/S treated HKMD with different hydration solutions after 56 days curing with temperature ranging from 40-900 °C are shown Fig. 8. Considering the complex composition of

307 the mixture, the possible products and their water loss temperatures were analysed. The weight loss of
308 each temperature range calculated from TG results are listed in Table 4.
309
310 The mass loss between 40-280 °C reflects the decomposition of hydration products including C-S-H,
311 AFt (Shen et al., 2017), M-S-H (Nied et al., 2016) and part of F's salt (200-350 °C) (Zhou et al., 2021)
312 due to the loss of their poorly-bound water, and the physically bonded water as well (Shen et al., 2017).
313 In this work, AFt loses its molecular water at 50-130 °C (Wang et al., 2004, Avet and Scrivener 2018)
314 with its peak around 100 °C, which was detected in all the samples with four mixing solutions.
315
316 Water in C/M-S-H was found to be both adsorbed water and hydroxyl groups within their structure
317 (Nied et al., 2016; Bernard et al., 2017). The weight loss from 280-720 °C is most likely related to: 1)
318 the water loss from $Ca(OH)_2$ (CH) between 380-600 °C (Wang et al., 2004; Alarcon-Ruiz et al., 2005;
319 Li et al., 2019); 2) the dehydroxylation of kaolinite from 400 °C to 600 °C (Avet and Scrivener, 2018);
320 3) the dihydroxylation of Ca–OH in C-S-H from 300-600 °C (Bernard et al., 2017); 4) the
321 dihydroxylation of Mg–OH in M-S-H at 400-750 °C (Bernard et al., 2019); and 5) the decarbonation of
322 $CaCO_3$ (CC) between 600-720 °C (Scrivener et al., 2017; Lu and Poon, 2018; Prochon and Piotrowski,
323 2020). Additionally, the remaining weight loss from 720-900 °C is suggested by Nied et al. (2016) as
324 silanol groups on M-S-H, or the inner OH groups in the crystallized M-S-H such as the talc structure
325 which dehydroxylates at 750 °C to 1000 °C (Dumas et al., 2013; Bernard et al., 2019) or the
326 dehydroxylates in crystallized C-S-H (Gallucci et al., 2013; Chakraborty et al., 2022).
327
328 From Fig. 8, it is shown that the largest proportion of weight loss and the steepest slope of the curve
329 occur at temperature above 280 °C. Especially for the peak with the centre at around 500 °C and 820
330 °C, the sample with $MgCl_2$ presents its maximum intensity in the DTG curve. It is mainly related to the
331 higher content of Mg in the mixture and thus of Mg-OH groups. In addition, from the DTG curves, it
332 seems that the treated samples with Na_2SO_4 solution have lower content of $Ca(OH)_2$ compared to the
333 other samples, and the samples with $MgCl_2$ solution have lower content of $CaCO_3$.

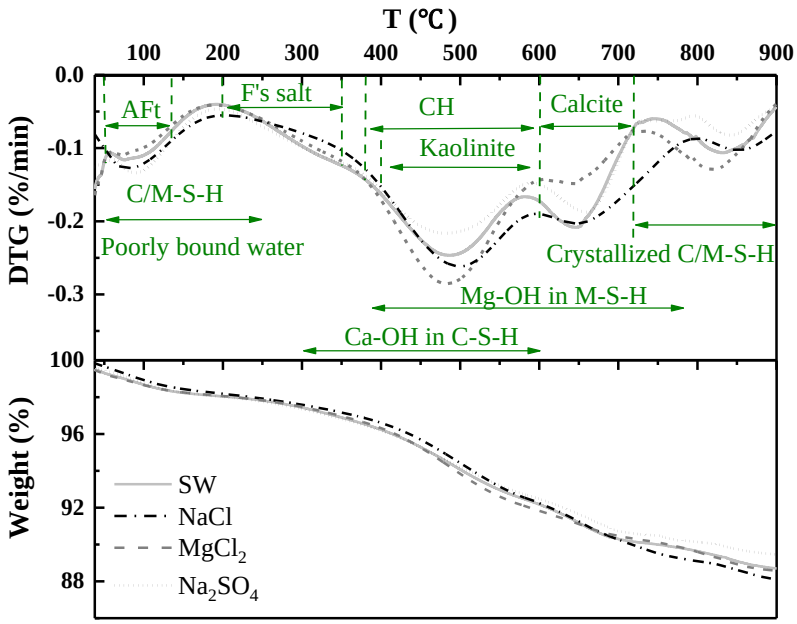

Fig. 8. TG and DTG curves of the treated samples after 56 days curing

Table 4. Weight loss of treated HKMD at 56 curing days when heated to 900 °C.

Solution	Weight loss (% of original)					
	30-200 °C	200-400 °C	400-600 °C	600-750 °C	750-900 °C	Total
SW	1.958	1.805	4.062	2.181	1.291	11.299
Na_2SO_4	1.987	1.839	3.698	1.993	1.028	10.545
NaCl	2.075	1.578	4.189	2.620	1.534	11.996
$MgCl_2$	1.937	1.745	4.489	1.721	1.526	11.419

3.4 MIP results

The microstructure property of the 56-day cured samples hydrated by four kinds of solutions was obtained by MIP method with the results presented in Fig. 9. It is observed that a unimodal pore structure distribution is presented with the dominant pore diameter of around 0.330 μm in the S/S samples. Besides, the number of pores in the mixtures with size of around 0.330 μm reduces with the hydration solution conditions in the order of Na_2SO_4>$MgCl_2$>SW>NaCl. The cumulative pore volume of treated samples after curing for 56 days is also shown in Fig. 9. It can be seen that the total pore volume is

different for different hydration solutions, which is following the condition order of Na_2SO_4>NaCl >SW>$MgCl_2$. It should be due to the part of pore volumes contributing from the pore diameter>30 μm, in which the pore volume in treated samples is the order of Na_2SO_4>NaCl >$MgCl_2$>SW.

To gain more insights into the PSD in the S/S treated HKMD samples, the pores were classified to four groups: 5-50 nm, 50 nm-2 μm, 2-10 μm, and >10 μm. Fig. 10 shows the four pore volumes in the S/S treated sediments with different mixing solutions at curing time of 28 and 56 days. The pore size from 5-50 nm for the first group is mainly contributed by the kaolinite particles in the HKMD (Yu et al., 2016) and the M-S-H aggregates (Tonelli et al., 2016; Dewitte et al., 2022). The pore size from 50 nm to 2 μm is partly due to the inter- aggregate pores in C-S-H and kaolinite, and partly due to the capillary pores (Zeng et al. 2012; Yu et al., 2016; Dewitte et al., 2022). Besides, the meso pores are assigned with diameters from 2-10 μm in the bulk samples. The biggest pore size group (> 10 μm) represents the air pores and cracks in the treated samples (Horpibulsuk et al., 2009; Dewitte et al., 2022). Due to the limitation of the MIP instrument, the nano pores from the C/M-S-H gels (1-5 nm) cannot be detected, and then the volume of the gel pores.

Because that the smallest sized pores (5-50 nm) partly represent the pores in the reaction products (M-S-H aggregates) in the mixture, it is obviously that the pore volume fraction of treated HKMD samples with $MgCl_2$ solution is highest, which confirms our judgment in turn. Curing time has little effect on this part of pore volume. The pore group with size from 50 nm to 2 μm in the treated samples with four solutions is the largest. As to the mesopore in the treated samples, the pore volume in the $MgCl_2$ mixed samples is the smallest. The volume of largest pore group increases in the samples with two sodium ion solutions with time, which suggests that the volume change is due to the increase of the number or size of the cracks. It can be also deduced that the reaction in the mixtures with curing time from 28 to 56 days, the C-S-H particles shrinkage leading to the increase of crack. The reason should be that the C-S-H particles have negative charges, which adsorbs Na^+ onto the surface of C-S-H particles (Sun et al., 2022). Besides, from Fig. 10 it can be also drawn that the effect of anions on porosity is less significant than that of cations.

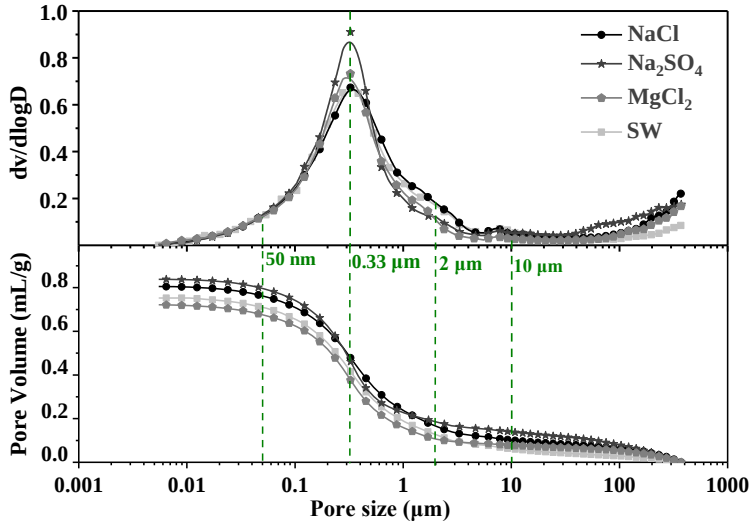

Fig. 9. MIP results for the samples after 56-day curing.

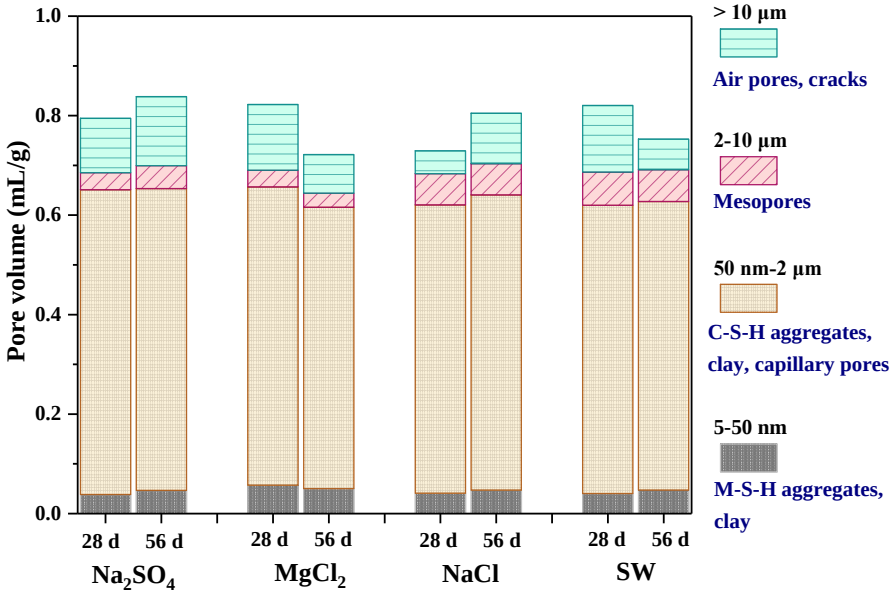

Fig. 10. Pore volume distribution of treated samples measured by MIP tests

3.5 NAI tests

Nitrogen adsorption/desorption isotherms tests were carried out to determine the nano-pores of equivalent diameter 1.7-45 nm in the treated HKMD powders after curing for 28 and 56 days. The SSA of treated HKMD were calculated by Brunauer-Emmett-Teller (BET) method. The BET SSA and average pore diameter of the samples with different mixing solutions are presented in Fig. 11. The differential and cumulative PSD obtained from the S/S treated HKMD samples with four mixing

386 solutions at 28 and 56 curing days are compared in Fig. 12, which was calculated by the Barrett-Joyner-
387 Halenda (BJH) theory.
388
389 From Fig. 11, it is clearly presented that the average pore diameter of the S/S treated HKMD powder
390 decreases while increasing the curing time from 28 to 56 days, except that of the sample hydrated by
391 Na_2SO_4 solution. On the contrary, the SSA value increases with the extension of curing time. It is also
392 shown that the SSA for the treated samples with the $MgCl_2$ mixing solution is highest and its average
393 diameter is lowest. At the same time, the SSA for the treated samples with the NaCl mixing solution is
394 lowest at the 28-curing day.
395 It is reported that in the cement paste almost all the SSA comes from C-S-H gels, and the development
396 of SSA is directly related to the content of C-S-H (Thomas et al., 1999; Garci Juenger and Jennings
397 2001; Pan et al., 2015). Additionally, the M-S-H gel was also proved to be a component with a high
398 SSA (Bernard et al., 2019). Thus, the development of the SSA in the S/S HKMD samples is mainly
399 related to the increase of C/M-S-H gel content. Due to the fact that such a character of SSA shown in
400 Fig. 12 is mainly associated with the C/M-S-H phases in the mixture, the content of C/M-S-H phases in
401 the treated samples with the $MgCl_2$ mixing solution is highest. Besides, the quantity of C/M-S-H
402 increasing with time should be due to continuing hydration (Garci Juenger and Jennings 2001).
403
404 The pore density of the treated HKMD samples hydrated by four solutions is presented in Fig. 12(a)
405 with its 1.5-5 nm part enlarged and shown in Fig. 12(b). From Fig. 12(a), it is obvious that the pore
406 density increases with the pore diameter ranging from 1.7 to 45 nm, and there is a peak at ~ 3 nm in pore
407 diameter. In addition, the pore density in the treated samples hydrated by $MgCl_2$ solution is higher than
408 that of the others at both 28 and 56 curing days. It is also found that the pores in the 56-day curing
409 samples are more than those in the 28-day curing samples. The peak of pore density at the pore diameter
410 from 1.7 to 4.7 nm in the treated samples is shown in Fig. 12(b). It is clearly that the pore density
411 increases significantly from pore diameters 1.7-3 nm, then it almost contains constant except in the case
412 of treated samples hydrated with NaCl solution. Among these curves, the pore density in the 56-day
413 $MgCl_2$ solution mixed sample highlights the obvious advantage of having more nano pores. From Fig.

12(c), the pore volume of treated HKMD calculated from NAI analysis using the BJH model increases in the pore diameter range of 1.7-45 nm.

As reported, the C-S-H globules allow the development of gel pores with the radius from 1 to 4 nm (Irico et al., 2013). It was investigated by Roosz et al. (2015) that the M-S-H had only nano meter-sized coherent scattering domains and the size of a coherent region of M-S-H was estimated at 1.5 - 2.4 nm in different planes. Similarly, Chiang et al. (2014) suggested a spherical structure for M-S-H with an average radius of 1.7 ± 1 nm. It was also reported that M-S-H samples exhibit a plate-like characteristic with pores < 50 nm (Sing et al., 1985; Bernard et al., 2019; Chevalier et al., 1994). Thus, it can be deduced that the peak emerges at the pore diameter from 1.7 to 4.7 nm should be due to the reaction products of C/M-S-H phases in the mixture. The results also indicate that the C/M-S-H phases in the 56-day treated samples are more than those in the 28-day samples, especially, the content of C/M-S-H phases in the samples of 56-day with $MgCl_2$ solution is highest. Therefore, a reasonable interpretation is that the increase of SSA and porosity indicates the promotion of hydration in the mixture. The pores with size of 1 nm - 10 nm) are primarily gel pores from C/M-S-H phases (Pan et al., 2015).

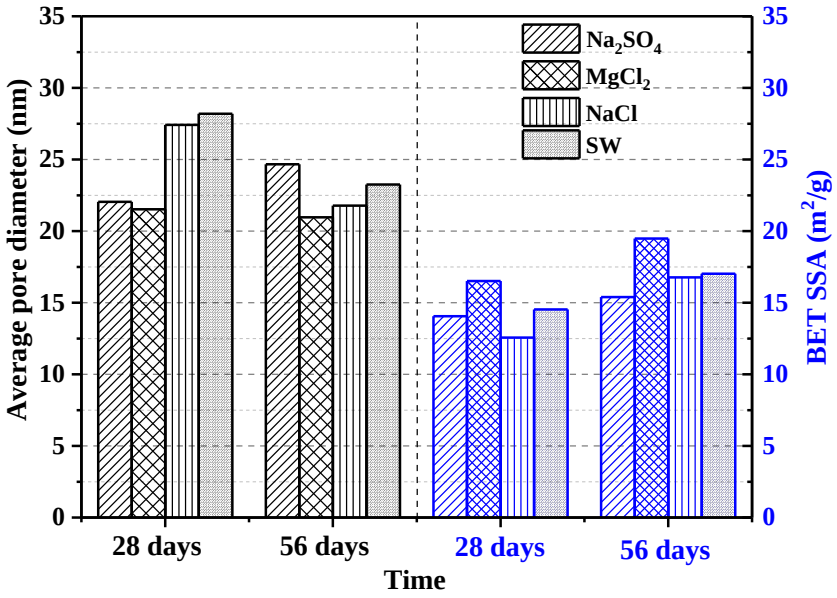

Fig. 11. The average pore diameter and SSA of treated samples from NAI tests.

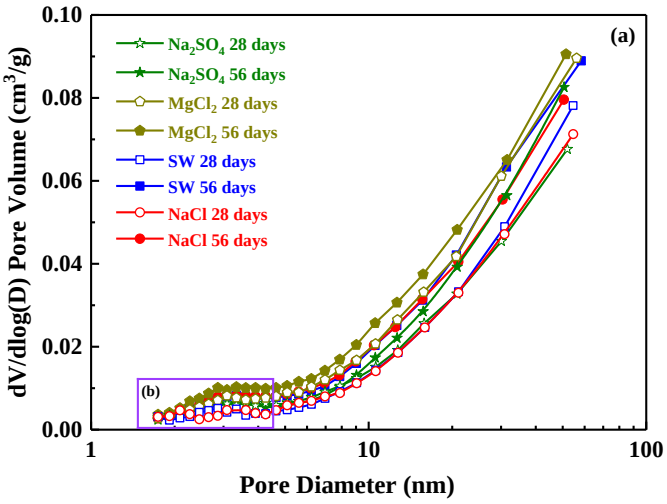

431

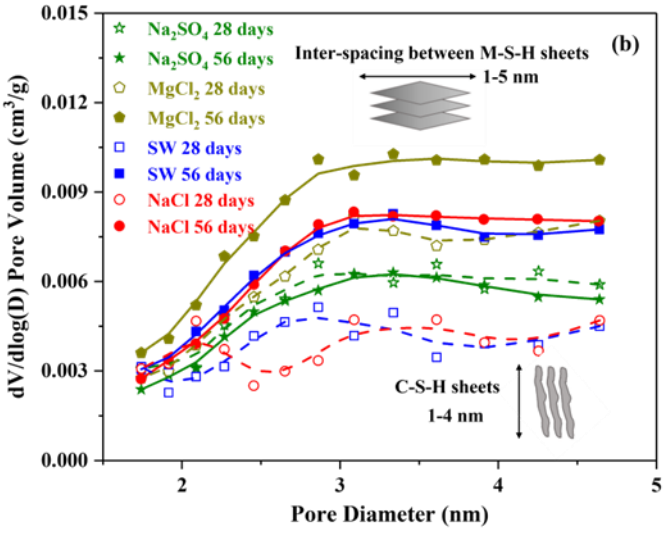

432

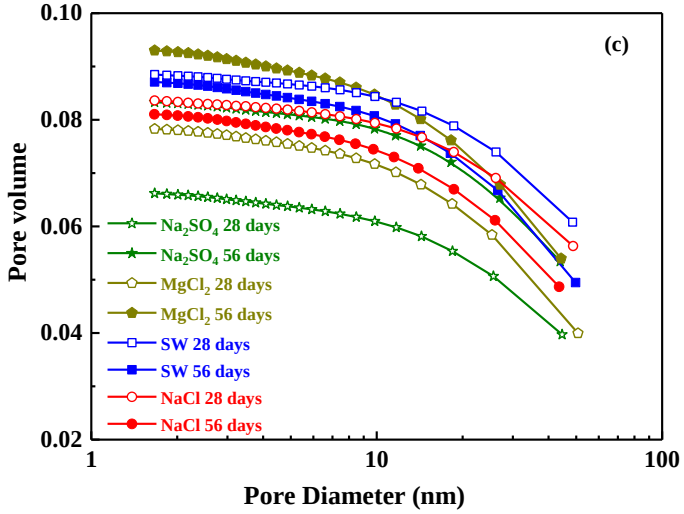

433

434 Fig. 12. The pore size distribution of treated HKMD samples.

435

3.6 SEM observations

The SEM micrograph with magnification of 5,000 and 10,000 for the 28- and 56- day curing samples prepared with different solutions are shown in Fig. 13, from which the morphological and microstructural characteristics of soil aggregates and the hydration products in the treated HKMD are clearly displayed. It can be noticed that the cracks and big pores are less in the 56-day curing sample than those in the 28-day sample. The microstructure and morphology of the 56-days sample with SW and $MgCl_2$ turn to be more homogeneous. A similar cracking phenomenon was found in the samples from Pan et al. (2015) and Dewitte et al. (2022), which was inferred due to the shrinkage of materials. The morphology of treated samples displays some needle shapes or fibrous clusters filling in the pores, which develop an extensive crystal interlocking the particles within the S/S samples. This can improve the strength and reduce the porosity of the mixture (Yuan et al., 2009; Jha and Sivapullaiah, 2016). It is seen that the HKMD particles are coated by precipitated gels, which indicates that the reactions occur in the lime-activated ISSA-GGBS binder treated HKMD materials and continue until the 56th curing day. Compared with the result of strength in Section 3.1, the reaction is still taking place at the 91st day, indicating a slow reaction speed.

The high magnification SEM micrograph clearly reveals the new needle-like or fibrillary phases and light-color gels coating on the surfaces of the mixture. More needle shapes or fibrous clusters are investigated in the samples hydrated by NaCl and Na_2SO_4 solutions. The needle-like or fibrillar morphology displays in the images can be identified as Aft type phase in agreement with the results reported by Han et al. (2012) and Bachtiar et al. (2022). In addition, the C-S-H looks like fibrillar, and the F's salt seems square mass. It was found that M-S-H did not show crystalline faces, but the globular chains (Dewitte et al., 2022). Because of the negative surface of M-S-H, a small particle size was observed (Bernard et al., 2019). The microscopic analysis by Tonelli et al. (2016) also confirmed the homogeneous M-S-H morphology and the globular nature of M-S-H particles.

In conclusion, the morphology and microstructure of the S/S treated HKMD samples are influenced by the compositions of hydration solutions. The use of different solutions leads to different features in homogeneity, morphology, and microstructure of the treated samples.

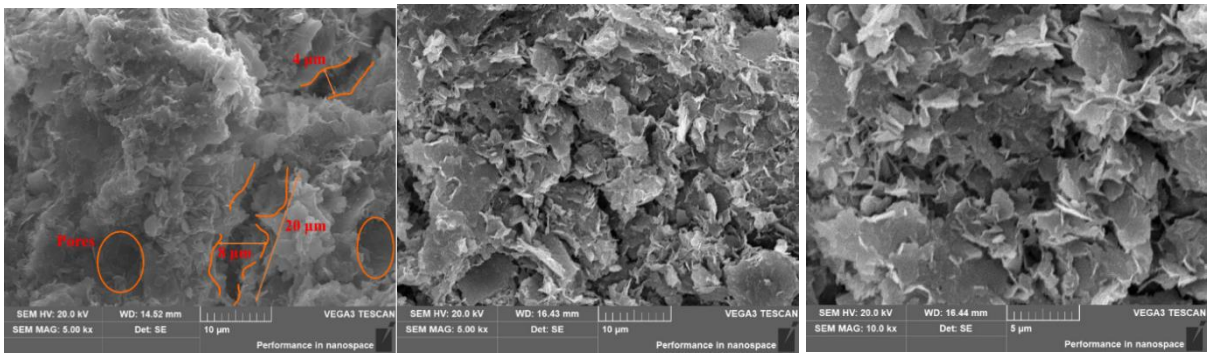

a1. SW-28 d-5 kx a2. SW-56 d-5 kx a3. SW-56 d-10 kx

(a) SW

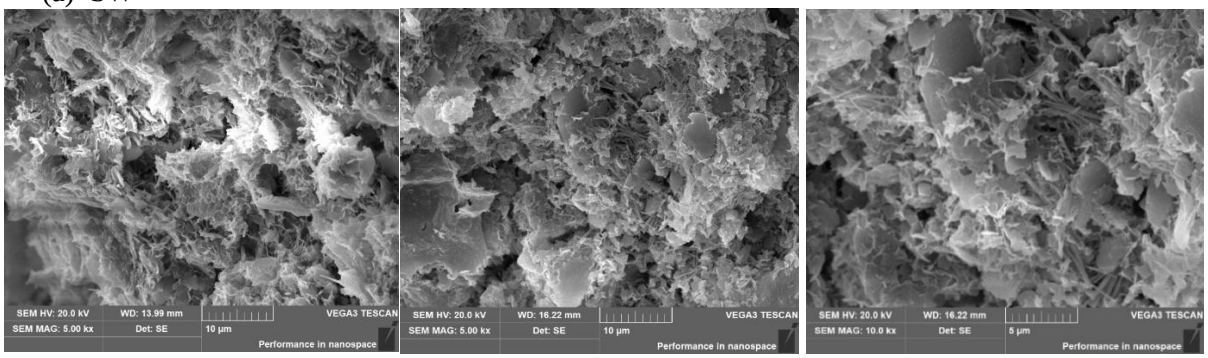

b1. NaCl – 28 d-5 kx b2. NaCl – 56 d-5 kx b3. NaCl – 56 d-10 kx

(b) NaCl

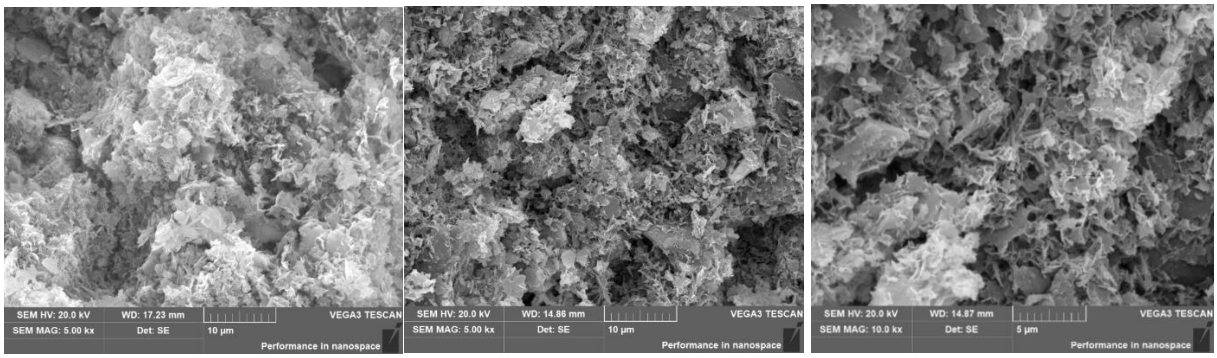

c1. $MgCl_2$ -28 d-5 kx c2. $MgCl_2$ -56 d-5 kx c3. $MgCl_2$ -56 d-10 kx

(c) $MgCl_2$

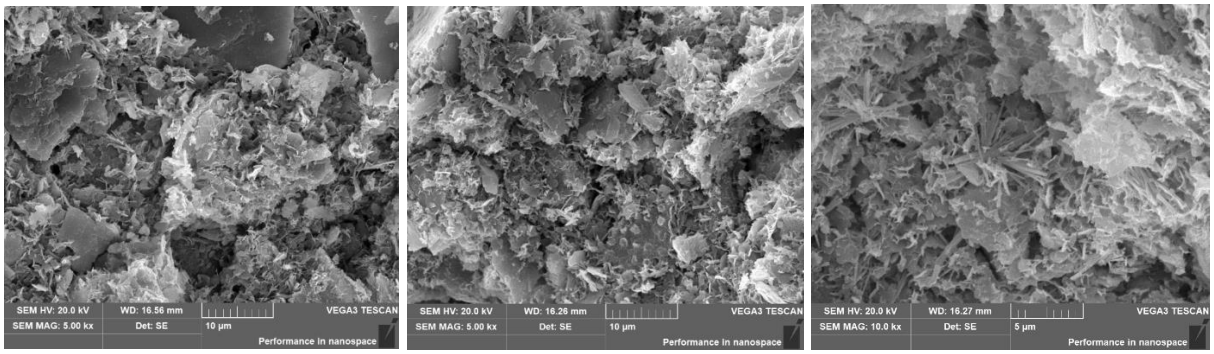

d1. Na_2SO_4 - 28 d d-5 kx d2. Na_2SO_4 - 56 d d-5 kx d3. Na_2SO_4 - 56 d d-10 kx

(d) Na_2SO_4

Fig. 13. SEM images of samples after different curing periods.

4 Discussions

4.1 Effect of chemical solutions on S/S treatment of HKMD

The research on S/S treatment of HKMD using CaO-activated industrial wastes (ISSA and GGBS) mixing with seawater is carried out in this work. In view of the variety of materials and chemical components, the reactions in the mixed system are quite complex. As the main cations in seawater are Na^+ and Mg^{2+}, and the main ions are Cl^- and SO_4^{2-}, the effects of NaCl, Na_2SO_4 and $MgCl_2$ on S/S treated HKMD were particularly studied. The XRD results reveal that the main reaction products in the mixture system are C-S-H, F's salt and AFt. According to Yonezawa et al. (1989), NaCl in the mixture would react with $Ca(OH)_2$ firstly forming $CaCl_2$ and NaOH. The $CaCl_2$ promotes cement hydrates forming C-S-H and then F's salt (Dehwah et al., 2003). As to Na_2SO_4 solution, Na_2SO_4 will react with $Ca(OH)_2$ forming $CaSO_4$, which will promote to form ettringite (Luo et al., 2019). The results from Brown and Badger (2000) show that the F's salt would convert to ettringite in the presence of a Na_2SO_4 solution, which indicates that the ettringite is a more stable phase in the reaction system. It was investigated by Kim et al. (2022) that $MgCl_2$ can lower the pH of the mixture and generate an environment more favourable to form M-S-H. Mg^{2+} reacts with OH^- to form $Mg(OH)_2$ initially, which continuously transfers to M-S-H (Sun et al., 2022). It was found that M-S-H could be formed by 1) the reaction between amorphous silica and $Mg(OH)_2$ (Gruyaert et al., 2012), 2) cement-based materials and clays (Dauzeres et al., 2010, 2016), and 3) the seawater infiltration in cement-based structures (Bonen and Cohen, 1991). It was detected a talc-like M-S-H phase on the XRD patterns (Mitsuda and Taguchi, 1977;

Dumas et al., 2013), which is in agreement with that in Nied et al. (2016). In fact, the M-S-H phase is hard to be detected due to its low crystalline and amorphous state (Martini et al., 2017; Roosz et al., 2015; Wang et al., 2019).

Besides, the brucite and portlandite as very important intermediate products during the hydration reactions in the system, their characteristic peaks were not detected by the XRD results, which is consistent with the observations in Wang et al. (2015) and Wang et al. (2019). The main reason should be that the identical patterns of these compositions in the mixtures are not sufficient to be detected by XRD. TG results and SEM results also confirm the new phases of C-S-H, F's salt and Aft. But due to the complex compositions in the mixture, it is hard to calculate the quantity of these crystalline and amorphous reaction products.

The water content changes of the treated HKMD samples with the four mixing solutions during the curing process are presented in Fig. 14. While the initial water content of HKMD is 110%, the water content of the HKMD after mixing with the binders is around 84%. From Fig. 14, a reduction in water content is observed in the treated samples with increasing curing time. From the slope of the curves, the water content loss is intense at the 0-28 days curing period, and then the water content decreases gently, which can reflect the reaction speed of the mixture to a certain extent. That is the reactions in the mixture are faster at the period of 0-28 days and the reaction rate gradually slows down from 28 to 91 days. The materials mixed with SW have a highest water content during the curing process. On the contrary, it is obvious that the sample mixing with $MgCl_2$ solution has a lowest water content at 28, 56 and 91 curing days. It can be inferred that the external water content decreases partly due to the deepening of internal reactions with the water consumed to generate new hydration products in the mixture.

It suggests that the chemical reactions in the S/S treated HKMD with $MgCl_2$ consume the most water. Associated with its highest SSA and the most of C/M-S-H phases in the reacted mixture (see Figs. 11 and 12(b)), the higher weight loss at 400-600 °C and 750-900 °C (Table 4), it can be inferred that M-S-H are formed in the treated samples with $MgCl_2$ together with the other hydrated phases and reaction

products in the mixture. From Bernard et al. (2018b), both M-S-H and C-S-H phases are stable and coexist at pH above 10. In addition, the presence of M-S-H was clearly detected in the calcium oxide and silica fume mixed sample with higher $MgCl_2$ contents, while at lower $MgCl_2$ contents (e.g., 9 g $MgCl_2$/200 g ($CaO+SiO_2$)) small quantities of M-S-H and mainly C-S-H presented (Bernard et al., 2017). In this work, there are more Mg^{2+} in SW and $MgCl_2$ solutions, which may result in the more homogeneous morphology and microstructure of the treated samples in Fig. 13. These may clearly suggest the M-S-H as the hydration phase.

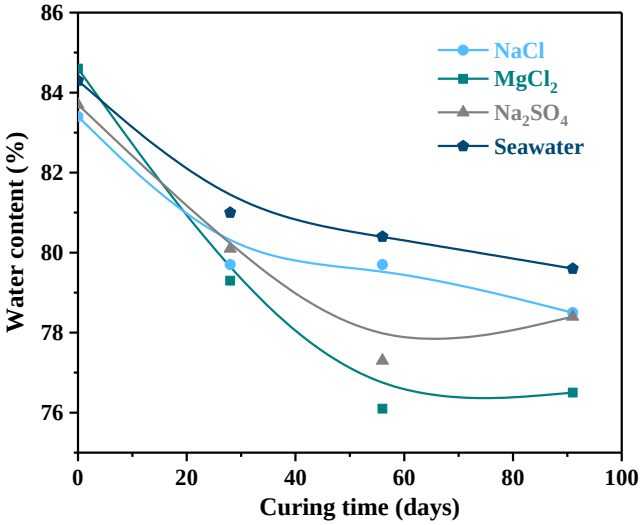

Fig. 14. The water content changes of treated samples with different curing periods

4.2 Effect of chemical solutions on microstructure

To analyse the nano-structure porosity in the ISSA-GGBS treated HKMD samples after mixing with the four solutions after 56 curing days, the pore volumes corresponding to pore diameters from 5-44 nm detected by MIP and NAI methods were analysed with the results presented in Fig. 15. The relationship between pore volume and pore diameter from both NAI and MIP methods is fitted with the linear curves as shown in Table 5. Since the samples for NAI analysis are in powder form, thus the pore volume obtained by NAI is from the material itself. As to the MIP analysis, the cumulative pore volume consists of the pore volume in the material and the bulk up volume of the block. To provide a quantitative analysis on the nano-structure in treated samples, the bulk up pore volume in the specimens is defined as:

$$V_{\text{bulk up volume}} = V_{\text{total}} - V_{\text{material}} \quad (3)$$

The total volume for the block sample detected by MIP method is estimated by the equation as follows:

$$\mathrm{V_{total}} = V_{44\ \mathrm{nm}}^{MIP} - V_{5\ \mathrm{nm}}^{MIP} = \Delta V_1 \quad (4)$$

where $V_{44\ \mathrm{nm}}^{MIP}$ is the cumulative pore volume at pore size of 44 nm in MIP tests; $V_{5\ \mathrm{nm}}^{MIP}$ is the cumulative pore volume at pore size of 5 nm in MIP tests calculated by linear fitting formula in Table 5.

The pore volume in the powder material is calculated by:

$$\mathrm{V_{material}} = V_{44\ \mathrm{nm}}^{NAI} - V_{5\ \mathrm{nm}}^{NAI} = \Delta V_2 \quad (5)$$

where $V_{44\ \mathrm{nm}}^{NAI}$ and $V_{5\ \mathrm{nm}}^{NAI}$ is the cumulative pore volume at pore size of 44 and 5 nm in NAI tests, respectively.

Therefore, the bulk up volume for the treated HKMD samples with four types of mixing solution can be estimated by:

$$\mathrm{V_{bulk\ up\ volume}} = \Delta \mathrm{V_1} - \Delta \mathrm{V_2} = \Delta V \quad (6)$$

It was reported that in cement-based materials the pores with diameters < 50 nm are mainly consisted of gel pores (< 10 nm) composed of pore system in C/M-S-H phases (Zhang et al., 2013; Pan et al., 2015) and inter-pores between the M-S-H aggregates (Tonelli et al., 2016; Dewitte et al., 2022). As to clays, the pores with size < 10 nm mostly locate in and between clay interlayers (Sasanian et al., 2013; Zong et al., 2015; Yu et al., 2016). From Fig. 15, it is clear that the bulk up volume ΔV is calculated as 0, 0.0066, 0.0082 and 0.0078 cm^3/g for samples with solution of $MgCl_2$, NaCl, Na_2SO_4 and SW, respectively. It shows that the nano-structure porosity in the material itself with $MgCl_2$ from NAI is the highest and the ΔV is the lowest. It means that the effect of $MgCl_2$ on the S/S treated HKMD results in refinement of the nano-structure with pores (5-45 nm) with an increasing pore volume (Wu et al., 2018), and there is almost no pore accumulation volume at <45 nm scale. This indicates that in the treated samples all pore volume comes from the material itself, that is, the nanoscale state and pore size distribution of the material are very uniform. The samples mixed with the other three solutions have bulk up volumes, and the two solutions containing sulfate (Na_2SO_4 and SW) have the highest nano-structure volumes. Considering the same salinity of solutions, the concentration of Cl^- is higher than that of SO_4^{2-}, which suggests that sulfate has a more significant effect on nano-pore size of sample porosity due to the stack of the mixture than chloride ion. It was in agreement with the findings that with the

usage of seawater replacing freshwater, the pore volume of pore diameter from 2 to 60 nm in cement paste increases (Wang et al., 2018). It is also reported that the impurity, salinity and chemical compositions of seawater have an effect on the pore structure of treated samples significantly (Zhao et al., 2021).

Table 5. Liner fitting curves of pore volume vs. pore diameter detected by NAI and MIP methods in the S/S HKMD.

Solution types	MIP			NAI		
	Intercept	Slope	R^2	Intercept	Slope	R^2
$MgCl_2$	0.845	-0.00089	0.986	0.094	-0.00091	0.998
NaCl	0.812	-0.00094	0.993	0.082	-0.00077	0.999
Na_2SO_4	0.846	-0.00093	0.988	0.085	-0.00072	0.999
SW	0.761	-0.00098	0.985	0.088	-0.00078	0.999

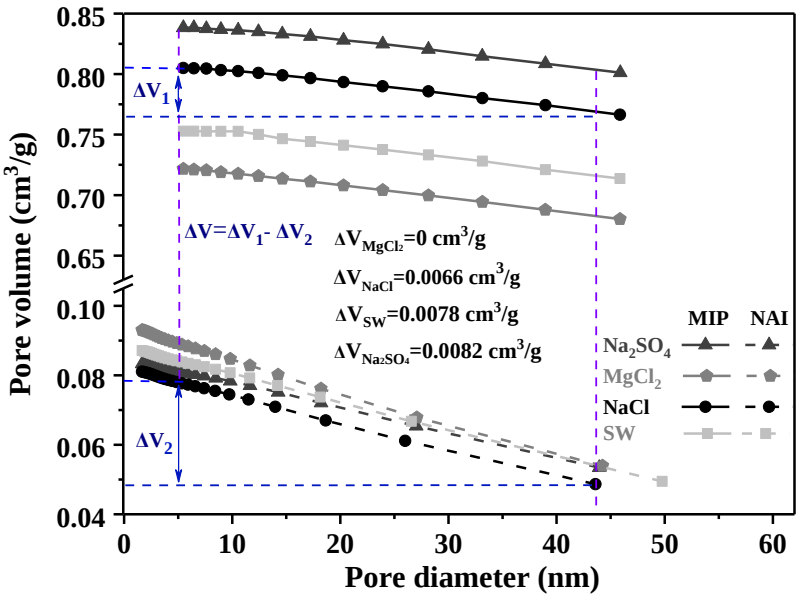

Fig. 15. Comparison of nano-pore volumes determined by NAI and MIP methods in 56 days treated samples

From MIP results in Fig. 10, it was found that the porosity for S/S treated HKMD samples mixing with Na_2SO_4 and NaCl increases with curing time, and it decreases with time in SW and $MgCl_2$ solutions, which is mainly due to the change of pore volume with pore diameter >10 μm in samples. That is the cracks or air pores (>10 μm) in samples mixing with Na_2SO_4 and NaCl increase with curing time, which can be confirmed by the SEM results in Fig. 13. In addition, the aggregate of mixture with Na_2SO_4 and NaCl is obviously bigger than that in cases of SW and $MgCl_2$ solutions. It may be because that the C-S-H particles in the mixture can adsorb Na^+ onto their surface and induce the aggregation of particles (Sun et al., 2022).

4.3 Effect of chemical solutions on strength

The lime-activated ISSA-GGBS treated HKMD slurry is indeed a complex system, while the main reactions are hydration reactions and pozzolanic reactions (Zhou et al., 2022). When the seawater is added, there would be two main effects of the compositions act on the S/S treatment, that is, positive and negative effects. From Fig. 4, the strength of samples follows the order of solution conditions of $MgCl_2$<SW< NaCl< Na_2SO_4, which indicates that the cation effect of Mg^{2+} on the soil strength is negative. Associated the lowest strength of treated sample with $MgCl_2$ in Figs. 4(a) and 6(a) with the maximum content of M-S-H in Figs. 10 and 12(b), it can be inferred that M-S-H phases in the lime-activated ISSA-GGBS binding HKMD samples has limited contribution in the strength improvement when comparing with that by C-S-H. Sun et al. (2022) found that the elastic modulus of C-S-H in alite pastes decrease when mixed with $MgCl_2$ solution, they thought it is mainly due to C-S-H decalcification and the M-S-H formation inducing the decrease of high-density C-S-H. In addition, the results of E_{50} presented in Fig. 6(b) suggest that even the strength increases in the samples with $MgCl_2$ and NaCl with time, the modulus of the samples almost keeps constant. It can be deduced that the increase of F's salt content in the treated soil has little effect on its modulus. In the same way, Na^+ acts a positive role in the strength improvement of S/S treated HKMD slurry (see Fig. 4). This may be because the negative charge on C-S-H particles in the mixture can adsorb Na^+ onto their surfaces, thereby improving the mechanical property of C-S-H (Sun et al., 2022).

As reported, pore structure is a main factor impacting the mechanical performance of cement-based materials (Sun et al., 2022). The use of seawater was found refining the pore structure by reducing the amounts of pores (10 nm-10 μm) (Li et al., 2015, Shi et al., 2015), especially for pores larger than 100 nm (Liu et al., 2016). While with the addition of $MgCl_2$, it formats a highly porous M-S-H with plate-like nano- and micro- pores (Dewitte et al., 2022), which leads to an optimization of pore structure and a reduced porosity, and thereby improved the strength (e.g., Tan et al., 2018; Zhang et al., 2018). While the strength of samples hydrated with $MgCl_2$ is the lowest, it indicates that M-S-H phases has limited contribution in the strength improvement when compared with that by C-S-H in these lime-activated ISSA-GGBS treated HKMD samples. It is suggested that seawater can facilitate strength gain of the dredged marine soft soil by stabilisation/solidification (S/S) technology with sustainable binding material, which solves the problem of insufficient bearing capacity of marine soft soil in marine geological engineering.

5 Conclusions

This work aims to investigate the effect of seawater and its compositions on the S/S performance of Hong Kong marine deposits (HKMD) treated lime-activated ISSA and GGBS in marine reclamation engineering. In view of the variety of materials and chemical components in the mixture, the reactions are complex. The S/S mechanism of HKMD by new sustainable binder hydrated by NaCl, Na_2SO_4, $MgCl_2$, seawater solutions with a salinity of 3.6% is studied based on multiple techniques including the XRD, TG, MIP, NAI, and SEM methods to analyse the mineralogy and microstructure characteristics. The results allow some conclusions to be drawn:

(1) The lime-activated industrial wastes (ISSA and GGBS) binder treated HKMD hydrated by seawater gains strength, and the strength increases with curing time. C/M-S-H, Friedel's salt, and ettringite are the main products, which are mainly responsible for the strength increase in S/S HKMD.

(2) The chemical compositions in seawater have different impacts on the performance of treated HKMD samples. Na^+ can help the treated HKMD samples gain higher strength, while increasing curing time, the cracks in the S/S treated samples will increase. Mg^{2+} in the mixture will lead to the M-S-H formation, which reduces the porosity of treated HKMD samples. However, the contribution of M-S-H to the soil strength is less than that of C-S-H. Cl^- has slight impacts on the sample modulus. Sulfate ion accelerates the reactions in the treated sample and has a more significant effect on nano- size of sample porosity than chloride ion.

To sum up, it is feasible to use seawater in S/S treatment of HKMD by improving its bearing capacity, but its composition may need to be adjusted, and the long-term performance of HKMD after treatment needs to be further studied.

Acknowledgements

This research was supported by the Research Grants Council of Hong Kong Special Administrative Region Government of China (Grant No.: R5037-18F and 15210322). The authors also acknowledge the financial supports from grants (CD7A and CD82) from Research Institute for Land and Space of Hong Kong Polytechnic University, and a grant (BD8U) from Hong Kong Polytechnic University.

Declaration of interests

The authors declare that they have no known competing financial interests or personal relationships that could have appeared to influence the work reported in this paper.

Authors' contributions

Zhao Sun: Testing, analysis, investigation, and writing; **Wenbo Chen**: Conceptualization, funding acquisition, methodology, review, and editing; **Rundong Zhao**: Testing, investigation; **Peiliang Shen**:

Methodology, review, and editing; **Jianhua Yin** and **Yong-gui Chen**: Supervision, project administration, review. All the authors commented on previous versions of the manuscript and approved the manuscript.

References

Alarcon-Ruiz, L., Platret, G., Massieu, E., Ehrlacher, A., 2005. The use of thermal analysis in assessing the effect of temperature on a cement paste. Cem. Concr. Res. 35 (3), 609–613.

Avet, F., Scrivener, K., 2018. Investigation of the calcined kaolinite content on the hydration of Limestone Calcined Clay Cement (LC3). Cement and Concrete Research 107, 124–135.

Bachtiar, E., Rachim, F., Makbul, R., Tata, A., Irfan-Ul-Hassan, M., Kirgiz, M. S., Syarif, M., de Sousa Galdino, A. G., Khitab, A., Benjeddou, O., Kolovos, K. G., Ledesma, E. F., Yusri, A., Papatzani, S., 2022. Monitoring of chloride and Friedel's salt, hydration components, and porosity in high-performance concrete. Case Studies in Construction Materials 17, e01208.

Bernard, E., Dauzères, A., Lothenbach, B., 2018a. Magnesium and calcium silicate hydrates, Part II: Mg-exchange at the interface "low-pH" cement and magnesium environment studied in a C-S-H and M-S-H model system. Applied Geochemistry 89, 210–218.

Bernard, E., Lothenbach, B., Cau-Dit-Coumes, C., Chlique, C., Dauzères, A., Pochard, I., 2018b. Magnesium and calcium silicate hydrates, Part I: Investigation of the possible magnesium incorporation in calcium silicate hydrate (C-S-H) and of the calcium in magnesium silicate hydrate (M-S-H. Applied Geochemistry 89, 229–242.

Bernard, E., Lothenbach, B., Chlique, C., Wyrzykowski, M., Dauzères, A., Pochard, I.8, Cau-Dit-Coumes, C., 2019. Characterization of magnesium silicate hydrate (M-S-H). Cement and Concrete Research 116, 309–330.

Bernard, E., Lothenbach, B., Le Goff, F., Pochard, I., Dauzères, A., 2017. Effect of magnesium on calcium silicate hydrate (C-S-H). Cement and Concrete Research 97, 61–72.

Bonen, D., Cohen, M.D., 1991. Magnesium sulfate attack on Portland cement paste - II. Chemical and mineralogical analyses. Cem. Concr. Res. 22, 707–718.

Brown, P.W., Badger, S., 2000. The distributions of bound sulfates and chlorides in concrete subjected to mixed NaCl, $MgSO_4$, Na_2SO_4 attack. Cem. Concr. Res. 30 (10), 1535–1542.

Celik, E., Nalbantoglu, Z., 2013. Effects of ground granulated blastfurnace slag (GGBS) on the swelling properties of lime-stabilized sulfate-bearing soils. Engineering Geology 163, 20–25.

Chakraborty, S., Puppala, A.J., Biswas, N., 2022. Role of crystalline silica admixture in mitigating ettringite-induced heavein lime-treated sulfate-rich soils. Géotechnique 72 (5), 438–454.

Cheng, Y., Li, Z.G., Huang, X., Bai, X.H., 2017. Effect of Friedel's salt on strength enhancement of stabilized chloride saline soil: Journal of Central South University, 24, 937-946.

Chevalier, S., Franck, R., Lambert, J., Barthomeuf, D.X, Suquet, H., 1994. Characterization of the porous structure and cracking activity of Al-pillared saponites. Appl. Catal. A Gen. 110, 153–165.

Chiang, W.-S., Ferraro, G., Fratini, E., Ridi, F., Yeh, Y.Q., Jeng, U., Chen, S.H., Baglioni, P., 2014. Multiscale structure of calcium-and magnesium-silicate-hydrate gels. J. Mater. Chem. A 2, 12991–12998.

Dauzeres, A., Achiedo, G., Nied, D., Bernard, E., Alahrache, S., Lothenbach, B., 2016. Magnesium perturbation in low-pH concretes placed in clayey environment–solid characterizations and modeling. Cem. Concr. Res. 79, 137–150.

Dauzeres, A., Bescop, P.Le., Sardini, P., Dit Coumes, C.Cau., 2010. Physico-chemical investigation of clayey/cement-based materials interaction in the context of geological waste disposal: Experimental approach and results. Cem. Concr. Res. 40, 1327–1340.

Dehwah, H.A.F., Maslehuddin, M., Austin, S.A., 2003. Effect of sulfate ions and associated cation type on the pore solution chemistry in chloride-contaminated plain and blended cements. Cement and Concrete Composites 25 (4-5), 513–525.

Dewitte, C., Bertron, A., Neji, M., Lacarriere, L., Dauzeres, A., 2022. Chemical and Microstructural Properties of Designed Cohesive M-S-H Pastes. Materials 15 (2), 547.

Dhondy, T., Remennikov, A., Shiekh, M.N., 2019. Benefits of using sea sand and seawater in concrete: A comprehensive review. Australian Journal of Structural Engineering 20 (4), 280−289.

Dumas, A., Martin, F., Roux, C.Le., Micoud, P., Petit, S., Ferrage, E., Brendlé, J., Grauby, O., Greenhill-Hooper, M., 2013. Phyllosilicates synthesis: a way of accessing edges contributions in NMR and FTIR spectroscopies. Example of synthetic talc. Phys. Chem. Miner. 40, 361–373.

Gallucci, E., Zhang, X., Scrivener, K. L., 2013. Effect of temperature on the microstructure of calcium silicate hydrate (C-S-H). Cement and Concrete Research 53, 185–195.
Garci Juenger, M.C., Jennings, H.M., 2001. The use of nitrogen adsorption to assess the microstructure of cement paste. Cem. Concr. Res. 31 (6), 883–892.
Gruyaert, E., Van Den Heede, P., Maes, M., De Belie, N., 2012. Investigation of the influence of blast-furnace slag on the resistance of concrete against organic acid or sulphate attack by means of accelerated degradation tests. Cem. Concr. Res. 42, 173–185.
Han, S., Yan, P., Liu, R., 2012. Study on the hydration product of cement in early age using TEM. Science China Technological Sciences 55 (8), 2284–2290.
Higgins, D.D., 2007. GGBS and sustainability. Constr. Mater. 160, 99–101.
HK CEDD., 2017. Model Specification for Soil Testing, Geospec3. Geotechnical Engineering Office. Civil Engineering and Development Department. https://www.cedd.gov.hk/filemanager/eng/content_122/es3_20170829.pdf.
Ho, T.O., Chen, W.B., Yin, J.H., Wu, P.C., Tsang, D.C.W., 2021. Stress-Strain behaviour of Cement-Stabilized Hong Kong marine deposits. Construction and Building Materials 274, 122103.
Horpibulsuk, S., Rachan, R., Raksachon, Y., 2009. Role of Fly Ash on Strength and Microstructure Development in Blended Cement Stabilized Silty Clay. Soils and Foundations 49 (1), 85–98.
Hunter, D., 1988. Lime-induced heave in sulfate-bearing clay soils. J. Geotech. Eng. 114(2), 150–167.
Irico, S., Gastaldi, D., Canonico, F., Magnacca, G., 2013. Investigation of the microstructural evolution of calcium sulfoaluminate cements by thermoporometry. Cement and Concrete Research 53, 239–247.
Jagaba, A.H., Shuaibu, A., Musa, S., Lawal, I.M., Abubakar, S., 2019. Stabilization of soft soil by incinerated sewage sludge ash from municipal wastewater treatment. Plant for Engineering Construction 2, 32–44.
Jenni, A., Mäder, U., Lerouge, C., Gaboreau, S., Schwyn, B., 2014. In situ interaction between different concretes and Opalinus clay. Phys. Chem. Earth A/B/C 70, 71–83.
Jha, A.K., Sivapullaiah, P.V., 2016. Volume change behavior of lime treated gypseous soil — influence of mineralogy and microstructure. Applied Clay Science 119, 202–212.
Kim, G., Im, S., Jee, H., Suh, H., Cho, S., Kanematsu, M., Morooka, S., Koyama, T., Nishio, Y., Machida, A., Kim, J., Bae, S., 2022. Effect of magnesium silicate hydrate (M-S-H) formation on the local atomic arrangements and mechanical properties of calcium silicate hydrate (C-S-H): In situ X-ray scattering study. Cement and Concrete Research 159, 106869.
Li, J.S., Zhou, Y.F., Wang, Q.M., Xue, Q., Poon, C.S., 2019. Development of a novel binder using lime and incinerated sewage sludge ash to stabilize and solidify contaminated marine sediments with high water content as a fill material. Journal of Materials in Civil Engineering. 31 (10), 04019245.
Li, Q., Geng, H., Shui, Z., Huang, Y., 2015. Effect of metakaolin addition and seawater mixing on the properties and hydration of concrete. Appl. Clay Sci. 115, 51–60.
Lin, D.F., Lin, K.L., Hung, M.J., Luo, H.L., 2007. Sludge ash/hydrated lime on the geotechnical properties of soft soil. J. Hazard Mater. 145, 58–64.
Liu, W., Cui, H., Dong, Z., Xing, F., Zhang, H., Lo, T.Y., 2016. Carbonation of concrete made with dredged marine sand and its effect on chloride binding. Constr. Build. Mater. 120, 1–9.
Lothenbach, B., Nied, D., L'Hôpital, E., Achiedo, G., Dauzères, A., 2015. Magnesium and calcium silicate hydrates. Cement and Concrete Research 77, 60–68.
Lu, J.X., Poon, C.S., 2018. Improvement of early-age properties for glass-cement mortar by adding nanosilica. Cement Concr. Compos. 89, 18–30.
Luo, Y., Zhou, S., Wang, C., Fang, Z., 2019. Effects of cations in sulfate on the thaumasite form of sulfate attack of cementitious materials. Construction and Building Materials 229, 116865.
Martini, F., Tonelli, M., Geppi, M., Ridi, F., Borsacchi, S., Calucci, L., 2017. Hydration of MgO/SiO2 and Portland cement mixtures: A structural investigation of the hydrated phases by means of X-ray diffraction and solid state NMR spectroscopy. Cement and Concrete Research 102, 60–67.
Min, X.B., Liu, D.G., Chai, L.Y., Ke, Y., Liang, Y.J., Shi, M.Q., Li, Y.C., Tang, C.J., Wang, Y.Y., Wang, Z.-B., 2019. Comparison of arsenic immobilization properties among calcium silicate hydrate, ettringite, and friedel's salt in a slag-based binder. Environmental Progress, Sustainable Energy 38 (s1), S422–S428.

Mitsuda, T., Taguchi, H., 1977. Formation of magnesiumsilicate hydrate and its crystallization to talc. Cem. Concr. Res. 7, 223–230.
Nied, D., Enemark-Rasmussen, K., L'Hopital, E., Skibsted, J., Lothenbach, B., 2016. Properties of magnesium silicate hydrates (M-S-H). Cement and Concrete Research 79, 323–332.
Nishida, T., Otsuki, N., Ohara, H., Garba-Say, Z.M., Nagata, T., 2015. Some considerations for applicability of seawater as mixing water in concrete. Journal of Materials in Civil Engineering 27 (7), B4014004.
Pan, S.C., Lin, C.C., Tseng, D.H., 2003. Reusing sewage sludge ash as adsorbent for copper removal from wastewater. Resour. Conserv. Recycl. 39, 79–90.
Pan, Z., He, L., Qiu, L., Korayem, A.H., Li, G., Zhu, J.W., Collins, F., Li, D., Duan, W. H., Wang, M.C., 2015. Mechanical properties and microstructure of a graphene oxide–cement composite. Cement and Concrete Composites 58, 140–147.
Prochon, P., Piotrowski, T., 2020. The effect of cement and aggregate type and w/c ratio on the bound water content and neutron shielding efficiency of concretes. Construction and Building Materials 264, 120210.
Roosz, C., Grangeon, S., Blanc, P., Montouillout, V., Lothenbach, B., Henocq, P., Giffaut, E., Vieillard, P., Gaboreau, S., 2015. Crystal structure of magnesium silicate hydrates (M-S-H): The relation with 2:1 Mg-Si phyllosilicates. Cement and Concrete Research 73, 228–237.
Sasanian, S., Newson, T.A., 2013. Use of mercury intrusion porosimetry for microstructural investigation of reconstituted clays at high water contents. Engineering Geology 158, 15–22.
Scrivener, K., Snellings, R., Lothenbach, B., 2017. A Practical Guide to Microstructural Analysis of Cementitious Materials. Taylor, Francis Group.
Shen, P., Lu, L., He, Y., Wang, F., Hu, S., 2017. Hydration of quaternary phase-gypsum system. Constr. Build. Mater. 152, 145–153.
Shi, Z., Shui, Z., Li, Q., Geng, H., 2015. Combined effect of metakaolin and sea water on performance and microstructures of concrete. Constr. Build. Mater. 74, 57–64.
Sun, Y., Lu, J.X., Poon, C.S., 2022. Strength degradation of seawater-mixed alite pastes: an explanation from statistical nanoindentation perspective. Cement and Concrete Research 152, 106669.
Tan, H., Zhang, X., He, X., Guo, Y., Deng, X., Su, Y., Wang, Y., 2018. Utilization of lithium slag by wet-grinding process to improve the early strength of sulphoaluminate cement paste. J. Cleaner Prod. 205, 536–551.
Thomas, J.J., Jennings, H.M., Allen, A.J., 1999. The Surface Area of Hardened Cement Paste as Measured by Various Techniques. Concr. Sci. Eng. 1 (1), 45–64.
Tonelli, M., Martini, F., Calucci, L., Fratini, E., Geppi, M., Ridi, F., Borsacchi, S., Baglioni, P., 2016. Structural Characterization of Magnesium Silicate Hydrate: Towards the Design of Eco-Sustainable Cements. Dalton Trans. 45, 3294–3304.
Wang, D., Gao, X., Wang, R., Larsson, S., Benzerzour, M., 2019. Elevated curing temperature-associated strength and mechanisms of reactive MgO-activated industrial by-products solidified soils: Marine Georesources, Geotechnology 38 (6), 659–671.
Wang, K., Shah, S.P., Mishulovich, A., 2004. Effects of curing temperature and NaOH addition on hydration and strength development of clinker-free CKD-fly ash binders, Cem Concr Res. 34 (2), 299–309.
Wang, L., Kwok, J.S.H., Tsang, D.C.W., Poon, C.S., 2015. Mixture design and treatment methods for recycling contaminated sediment. J. Hazard Mater. 283, 623–632.
Wang, J., Liu, E., Li, L., 2018. Multiscale investigations on hydration mechanisms in seawater OPC paste: Construction and Building Materials 191, 891-903.
Wild, S., Kinuthia, J.M., Jones, G.I., 1998. Suppression of swelling associated with ettringite formation in lime stabilized sulphate bearing clay soils by partial substitution of lime with GGBS. Engineering Geology 51 (4), 257–277.
Wu, Z., Shi, C., Khayat, K.H., (2018. Multi-scale investigation of microstructure, fiber pullout behavior, and mechanical properties of ultra-high performance concrete with nano-CaCO3 particles. Cement and Concrete Composites 86, 255–265.
Xu, J., Zhang, C., Jiang, L., Tang, L., Gao, G., Xu, Y., 2013. Releases of bound chlorides from chloride-admixed plain and blended cement pastes subjected to sulfate attacks. Construction and Building Materials 45, 53–59.

Yi, Y., Li, C., Liu, S., Al-Tabbaa, A., 2014. Resistance of MgO–GGBS and CS–GGBS stabilised marine soft clays to sodium sulfate attack. Geotechnique 64 (8), 673–679.
Yi, Y.L., Gu, L.Y., Liu, S., 2015. Microstructural and mechanical properties of marine soft clay stabilized by lime-activated ground granulated blast furnace slag: Applied Clay Science 103, 71-76.
Yonezawa, T., Ashworth, V., Procter, RPM., 1989. The Mechanism of fixing Cl by Cement Hydrates resulting in the transformation of NaCl to NaOH. Proceedings of the 8th International Conference on Alkali-Aggregate Reaction. Kyoto, 153–160.
Younis, A., Ebead, U., Suraneni, P., Nanni, A., 2018. Fresh and hardened properties of seawater-mixed concrete. Construction, Building Materials 190, 276–286.
Yu, C.Y., Chow, J.K., Wang, Y.H., 2016. Pore-size changes and responses of kaolinite with different structures subject to consolidation and shearing. Engineering Geology 202, 122–131.
Yuan, Q., Shi, C., De Schutter, G., Audenaert, K., Deng, D., 2009. Chloride binding of cement-based materials subjected to external chloride environment – a review. Construct. Build. Mater. 23 (1), 1–13.
Zeng, Q., Li, K.F., Chong, T.F., Dangla, P., 2012. Pore structure characterization of cement pastes blended with high-volume fly-ash. Cem. Concr. Res. 42, 194–204.
Zentar, R., Wang, D., Abriak, N.E., Benzerzour, M., Chen, W., 2012. Utilization of siliceous–aluminous fly ash and cement for solidification of marine sediments. Construct. Build. Mater. 35, 856–863.
Zhang, P., Dai, Y., Ding, X., Zhou, C., Xue, X., Zhao, T., 2018. Self-healing behaviour of multiple microcracks of strain hardening cementitious composites (SHCC). Constr. Build. Mater. 169, 705–715.
Zhang, Q., Ye, G., Koenders, E., 2013. Investigation of the structure of heated Portland cement paste by using various techniques. Construction and Building Materials 38, 1040–1050.
Zhao, Y., Hu, X., Shi, C., Zhang, Z., Zhu, D., 2021. A review on seawater sea-sand concrete: Mixture proportion, hydration, microstructure and properties. Construction and Building Materials 295, 123602.
Zhou, Y., Cai, G., Cheeseman, C., Li, J., Poon, C.S., 2022. Sewage sludge ash-incorporated stabilisation/solidification for recycling and remediation of marine sediments. Journal of Environment Management 301, 113877.
Zhou, Y., Lu, J., Li, J., Cheeseman, C., Poon, C.S., 2021b. Influence of seawater on the mechanical and microstructural properties of lime-incineration sewage sludge ash pastes. Construction and Building Materials 278, 122364.
Zhou, Y., Lu, J., Li, J., Cheeseman, C., Poon, C.S., 2021a. Hydration, mechanical properties and microstructure of lime-pozzolana pastes by recycling waste sludge ash under marine environment. Journal of Cleaner Production 310, 127441.
Zong, Y., Yu, X., Zhu, M., Lu, S., 2015. Characterizing soil pore structure using nitrogen adsorption, mercury intrusion porosimetry, and synchrotron-radiation-based X-ray computed microtomography techniques. Journal of Soils and Sediments 15 (2), 302–312.